Influence of Sintering Conditions on the Structure and Redox Speciation of Homogeneous (U,Ce)O2+δ Ceramics: A Synchrotron Study

Malvina Massonnet, Laurent Claparede, Julien Martinez, Philippe Martin, Myrtille O.J.Y. Hunault, Damien Prieur, Adel Mesbah, Nicolas Dacheux, Nicolas Clavier

Influence of sintering conditions on the structure and the redox speciation of homogenous (U,Ce)O$_{2+\delta}$ ceramics : a synchrotron study

Malvina Massonnet [1], Laurent Claparede [1], Julien Martinez [2], Philippe Martin [2], Myrtille O.J.Y. Hunault [3], Damien Prieur [4,5], Adel Mesbah [1,6], Nicolas Dacheux [1], Nicolas Clavier [1,]*

[1]   ICSM, Univ Montpellier, CEA, CNRS, ENSCM, Bagnols/Cèze, France

[2]   CEA, DES, ISEC, DMRC, Univ Montpellier, Marcoule, France

[3]   Synchrotron SOLEIL, L'Orme des Merisiers, Départementale 128, 91190 Saint-Aubin, France

[4]   Institute of Resource Ecology, Helmholtz Zentrum Dresden-Rossendorf (HZDR), 01314 Dresden, Germany

[5]   The Rossendorf Beamline at ESRF - The European Synchrotron, 38043 Grenoble Cedex 9, France

[6]   Univ Lyon, Université Claude Bernard Lyon 1, CNRS, IRCELYON, 69626 Villeurbanne, France

* Corresponding author:

Dr. Nicolas CLAVIER
ICSM, Univ Montpellier, CEA, CNRS, ENSCM
Site de Marcoule
BP 17171
30207 Bagnols sur Cèze
France

Phone : + 33 4 66 33 92 08
Fax : + 33 4 66 79 76 11

nicolas.clavier@icsm.fr

Abstract :

Although uranium-cerium dioxides are frequently used as surrogate material for $(U,Pu)O_{2-\delta}$ nuclear fuels, there is currently no reliable data regarding the oxygen stoichiometry and the redox speciation of the cations in such samples. In order to fill this gap, this manuscript details a synchrotron study of highly homogeneous $(U,Ce)O_{2\pm\delta}$ sintered samples prepared by wet-chemistry route. HERFD-XANES spectroscopy led to determine accurately the O/M ratios (with M = U + Ce). Under reducing atmosphere ($pO_2 \approx 6\times10^{-29}$ atm at 650°C), the oxides were found close to O/M = 2.00 while the O/M ratio varied with the sintering conditions under argon ($pO_2 \approx 3\times10^{-6}$ atm at 650°C). They globally appear to be hyper-stoichiometric (*i.e.* O/M > 2.00), the departure from the dioxide stoichiometry decreasing with both the cerium content in the sample, and the sintering temperature. Nevertheless, such deviation from the ideal O/M = 2.00 ratio was found to generate only moderate structural disorder from EXAFS data at the U-L$_3$ edge, as all the samples retained the fluorite-type structure of the UO$_2$ and CeO$_2$ parent compounds. The determination of accurate lattice parameters thanks to S-PXRD measurements led to complement the data reported in the literature by various authors. These data were consistent with an empirical relation linking the unit cell parameter, the chemical composition and the O/M stoichiometry, showing that this latter can be evaluated simply within a ± 0.02 uncertainty.

Keywords: uranium oxide ; XAS ; structure ; nuclear fuel ; O/M ratio

1. Introduction

Uranium-plutonium mixed dioxides $(U,Pu)O_{2-\delta}$ are currently used as fuels in several pressurized-water reactors worldwide, and constitute one of the reference fuels for some of the concepts developed for the fourth generation of nuclear reactors, such as sodium-cooled fast reactor (SFR) [1]. While some countries (e.g. France) already chosed to reprocess UOx spent fuel in order to minimize the radiotoxicity of ultimate wastes and to save resources [2], the spent $(U,Pu)O_{2-\delta}$ assemblies are currently stored, pending for a solution of storage or reprocessing. This latter option is now envisaged in France, with the aim to refabricate new fuel elements, and then to stabilize the plutonium stockpile [3].

Such a process first implies to master the quantitative dissolution of the $(U,Pu)O_{2-\delta}$ spent fuel, which is a mandatory step before any operation of partitioning. Nevertheless, if the dissolution of UO_x has been extensively documented [4-11], that of $(U,Pu)O_{2-\delta}$ mixed oxides remains less understood, partly due to the high specific activity of plutonium that restrains the possibilities of the study [12-14]. Especially, only few works discussed the impact of the microstructural parameters on the dissolution rate in acidic media [15]. Furthermore, the links between dissolution rate and the cation redox speciation in the solid are generally not studied. These latter are of particular importance owing to the complex redox properties of actinide cations. Indeed, while uranium and plutonium are mainly tetravalent in the pristine fuel, they can endure either oxidation or reduction during irradiation, respectively. Also, the presence of aliovalent cations such as soluble fission products (Nd, La, …) into the UO_2 matrix is expected to impact the uranium redox speciation. As a result, the fuel matrix mainly consists of a mixture of U(IV), U(V) and even U(VI), on the one hand, and Pu(IV) and Pu(III) on the other, which gives rise to a large variety of O/M ratios (with M = U+Pu) [16, 17].

As tetravalent plutonium, cerium (IV) exhibits a complete solubility into the UO_2 fluorite-type structure, and $(U,Ce)O_{2\pm\delta}$ oxides are frequently considered as model compounds for $(U,Pu)O_{2\pm\delta}$ fuels [18]. Even if they do not constitute perfect surrogates, for example due to differences in the U-Ce-O and U-Pu-O ternary phase diagrams, cerium still possesses similar stable oxidation states than plutonium in oxide compounds, as well as close ionic radius in the eight-fold coordination (0.97 Å for Ce(IV) vs. 0.96 Å for Pu(IV)) [19]. Hence, some efforts have been made both to prepare uranium-cerium dioxides samples with different morphologies (including nanopowders, thin films or dense pellets) [20-23] and in some cases to investigate their behavior during dissolution tests [24]. In such studies, several biases can be pointed out, and

preclude a reliable determination of the sample oxygen stoichiometry, expressed through the O/M ratio with M = U + Ce.

Most of the authors assumed that uranium and cerium remained tetravalent all along the fabrication process of the samples, without bringing any experimental evidence. Also, the differences in both the fabrication method, the samples morphology, and the techniques used to determine the O/M ratio, can lead to a limited representativity of the results. Indeed, powder metallurgy processes were frequently used to manufacture the samples, which is now well-known to induce heterogeneities in the cation distribution that can localy induce an incomplete formation of the $(U,Ce)O_{2\pm\delta}$ solid solution (*i.e.* out-of-equilibrium systems) [25]. Similarly, the investigation of thin films or nanosized powders, as well as the use of surface techniques such as X-ray Photoelectron Spectroscopy (XPS) can increase the sensitivity of the samples towards surface oxidation [22, 26].

In the prospect of using uranium-cerium dioxide as a surrogate material, its density has to be as close as possible to those encountered in the fuel, *i.e.* about 95% of the theroretical density. Such value is generally achieved through a sintering process based on a thermal treatment at high temperature (around 1700°C) in a controled reducing atmosphere. However, there is currently no reliable data regarding the oxygen stoichiometry and the redox speciation of the cations in $(U,Ce)O_{2\pm\delta}$ dense samples, that can be used to link the sintering process parameters (including temperature, duration and oxygen partiel pressure) with the final microstructural and structural properties of the ceramics. In order to fill this gap, this manuscript describes a synchrotron study of highly homogeneous $(U,Ce)O_{2\pm\delta}$ samples. These latter were obtained from nanometric powders prepared by wet chemistry method, already presenting a homogenous distribution of the cations at the sub-micronic scale and a very high specific surface area. These characteristics ensured the fast diffusion of cations in the solid during heat treatements, then the rapid formation of solid solutions at the equilibrium state. The structural long and short range orders of the samples were then explored by coupling Synchrotron Powder X-Ray Diffraction (S-PXRD) and Extended X-ray Absorption Fine Structure (EXAFS) spectroscopy. The redox speciation of the cations was determined by HERFD-XANES (High Energy Resolution Fluorescence Detected – X-ray Absorption Near Edge Spectroscopy).

4

2. Experimental

Preparation of the powdered samples and sintering. The synthesis of the $(U,Ce)O_{2\pm\delta}$ starting powders was adapted from the protocol initially reported by Martinez *et al.* [21], and based on the precipitation and rapid ageing of mixed hydroxides. All the usual chemicals were supplied by Merck and were of analytical grade, while uranium was kindly provided by CETAMA under the form of metal chips. In a first step, uranium metal pieces were dissolved in concentrated hydrochloric acid (6M) to obtain a 0.5M U(IV) solution following the protocol already described in our previous publications [27]. A second solution containing Ce(IV) was obtained from the dissolution of cerium sulfate salt in HCl. These two solutions were mixed in the desired molar ratio (i.e. $x_{Ce} = \frac{Ce}{U+Ce} = 0.15$, 0.25 and 0.50), then poured in a large excess of 2M NH_3 (about 400%) under magnetic stirring, resulting in the immediate formation of a $(U,Ce)(OH)_4$ precipitate. This latter was let under stirring for 30 minutes, in order to favour the grain growth and ageing into the $(U,Ce)O_2.nH_2O$ form [28]. The precipitate was then separated from the supernatant by centrifugation at 14000 rpm during 10 minutes, and washed twice with deionized water and once with ethanol. It was finally dried at room temperature in an inert glovebox filled with argon (O_2 content below 0.1 ppm) then calcined at 700°C for 4 hours under Ar/H_2 4% in order to eliminate volatile compounds remaining from the synthesis process.

The accurate chemical composition of the samples was further determined through the complete dissolution of a fraction of powder in aqua regia, followed by the measurements of U and Ce concentrations in the resulting solutions by Inductively-Coupled Plasma Atomic Emission Spectroscopy (ICP-AES, Spectro Arcos). For each composition considered, an average of U and Ce measurements was made at different wavelengths (i.e. $\lambda = 448.691$ nm, 418.660 nm, 413.765 nm and 413.380 nm for cerium and $\lambda = 385.958$ nm, 409.014 nm, 367.007 nm and 279.394 nm for uranium), and led to $x_{Ce} = \frac{Ce}{U+Ce}$ molar ratios equal to 0.14; 0.26 and 0.49, respectively. These values confirmed the quantitative precipitation of both cations during the synthesis, as expected from previous results [21]. They will be used therafter to label the samples studied.

Before sintering, the powders were sieved (200 μm mesh) and shaped as 5 mm diameter pellets by uniaxial pressing (500 MPa) at room temperature. The obtained green pellets (showing a mass of about 200 mg) were then sintered in various operating conditions in terms of temperature, heat treatment duration and atmosphere. For this latter, two options were

considered, to establish either reducing (Ar/H$_2$ 4%) or slightly oxidant (Ar) conditions in the furnace. In both cases, the corresponding oxygen partial pressure was measured by a Setnag Jok'air analyzer (internal furnace set at 650°C), leading to values close to pO$_2$ ≈ 6×10^{-29} atm and pO$_2$ ≈ 3×10^{-6} atm, respectively. The different samples prepared are summarized in **Table 1**. In all the cases, heating rates of 2°C.min^{-1} were considered, with a cooling rate of 6°C.min^{-1}. It is also to note that, due to equipment constraints, it was not possible to maintain a temperature plateau at T = 1600°C, this temperature being only briefly reached by the furnace. For simplification purposes, the holding time is then indicated to be equal to zero in the following. In these conditions, the samples might not have reached thermal equilibrium, even if the slow heating rate guaranteed a sample temperature close to 1600°C. Nevertheless, datapoints obtained at this temperature were analyzed with caution, owing to the potential differences in sintering and redox kinetics compared to the others.

Table 1.   Sintering conditions applied to the U$_{1-x}$Ce$_x$O$_{2+\delta}$ powder samples during this study.

x$_{Ce}$	Sintering temperature (°C)	Holding time (hours)	Atmosphere
0.14	1400	10	Ar
	1600	0	Ar
	1400	10	Ar/H$_2$ 4%
	1600	0	Ar/H$_2$ 4%
0.26	1300	10	Ar
	1400	10	Ar
	1500	10	Ar
	1600	0	Ar
	1300	10	Ar/H$_2$ 4%
	1400	10	Ar/H$_2$ 4%
	1500	10	Ar/H$_2$ 4%
	1600	0	Ar/H$_2$ 4%
0.49	1400	10	Ar
	1600	0	Ar
	1400	10	Ar/H$_2$ 4%
	1600	0	Ar/H$_2$ 4%

SEM observations and statistical EDS analyses. SEM observations were carried out on pristine samples using a FEI Quanta 200 ESEM FEG microscope equipped with a Large Field Detector (LFD) and a Back-Scattered Electron Detector (BSED). A low acceleration voltage of 5-10 kV coupled with low vacuum conditions (i.e. 50 Pa water vapor) was chosen to

observe the samples without any additional preparation step such as metallization. Additionally, statistical EDS measurements were conducted in order to point out the distribution of the $\frac{Ce}{U+Ce}$ molar ratio in the samples. With this aim, the powders were pressed as 5mm-diameter discs to achieve a flat surface aiming to obtain semi-quantitative data, while UO_2 and $CePO_4$ were used as standards. Around 100 analyses were then recorded at different locations of the pellet's surface.

X-Ray Diffraction. Synchrotron Powder X-Ray Diffraction (S-PXRD) were performed at the European Synchrotron Radiation Facility (ESRF, Grenoble) on the HZDR-operated Rossendorf Beamline (BM20). S-PXRD data were recorded using a Pilatus3X 2Mdetector (Dectris Ltd.), on 0.5 mg of ground powder in a rotating quartz capillary (inner diameter of 0.2 mm). Calibration was performed using a LaB_6 standard and the sample to detector distance was equal to 36 cm. The excitation energy was set at 17038 eV, below the U L_3 absorption edge to avoid scattering background due to the fluorescence.

Synchrotron measurements were complemented by laboratory Powder X-Ray Diffraction (PXRD) using a Bruker D8 diffractometer equipped with a Lynxeye detector in the reflection geometry with Göbel mirror and using Cu $K\alpha_{1,2}$ radiation ($\lambda_{average}$ = 1.54184 Å). PXRD patterns were recorded at room temperature in the $5 - 100°$ range (2θ), a step size of $\Delta(2\theta)$ = 0.02° and a total counting time of about 3 hours per sample. In order to avoid any radioactive contamination, the powders were placed in a special sample holder, composed by a dome-shaped container with anti-scattering blade and an austenite steel plate, also containing trace amounts of ferrite. The first could generate an additional large peak between 10 and 20° (2θ), while the second could occasionate small intensity diffraction lines, notably around $2\theta = 43$ and 50° (see PDF file 00-023-0298).

The diffraction patterns obtained from both data series were refined by the Rietveld method to extract unit cell parameters and average crystallite sizes, using the Cox-Hastings pseudo-Voigt profile function [29] implemented in the Fullprof_suite program [30].

HERFD-XANES. High-energy resolution fluorescence detected XANES (HERFD-XANES) data were measured at the MARS beamline of the SOLEIL synchrotron (Saint-Aubin, France) [31, 32]. The storage ring was operating in top-up mode at an electron current of 500 mA, 2.5 GeV. The beam size on sample was 150 μm × 150 μm FWHM (H×V). Spectra were measured at the U M_4-edge (3728 eV) and the Ce L_3-edge (5723 eV) using the double-crystal

monochromator (DCM) equiped with a pair of Si(111) crystals. Higher harmonics rejection and vertical focusing was achieved using the Si strip of each mirror inserted before and after the DCM with a 4 mrad incidence angle. The incident energy was calibrated using the absorption K-edge of potassium of a KBr pellet (3608.4 eV). The incident X-ray flux on the sample position was 1.9×10^9 ph/s at 3.5 keV. HERFD-XANES was measured using the crystal-analyzer emission spectrometer in the Rowland geometry and a KETEK single element silicon solid state detector. The M_β emission line of U (3339 eV) was analyzed using the 220 reflection of a Si(220) bent diced crystal analyzer with a curvature radius of 1 meter. The energy resolution of the emission spectrometer was 0.55 eV. The L_α emission line of Ce (4839.2 eV) was analysed using a Ge(331) bent cristal analyser. The energy resolution of the emission spectrometer was 0.89 eV. The samples were oriented at 45° with respect to the incident beam. A He-filled balloon was used to reduce the scattering of the incident and emitted X-rays by the air between the sample and the crystal analyzer and the detector. Samples were prepared as pellets for each compound diluted in boron nitride. All spectra collected were normalized at the maximum of absorption using the Athena Software [33], then were fitted as a linear combination of different references to quantify the contribution of U(IV), U(V) and U(VI), on the one hand, and of Ce(IV) and Ce(III), on the other.

For uranium, a $UO_{2.00}$ single crystal was chosen as pure U(IV) standard, while a U_4O_9 spectrum previously collected at the ESRF-ID26 beamline was used as a mixed standard for U(IV)/U(V) with a 1/1 ratio [34]. Additionally, U_3O_8 was taken as a mixed standard for U(V)/U(VI) with a 2/1 ratio [34] while $UO_2(NO_3)_2\cdot5H_2O$ was selected as pure U(VI) standard. For cerium, CeO_2 and $CePO_4$ were chosen as references for Ce(IV) and Ce(III), respectively. All fits were obtained with a quality factor of $X^2 < 0.04$.

From the linear combination results, it was then possible to determine the different O/M molar ratios as follows :

$$O/U = mol.\%(UO_2) \times 2 + mol.\%(U_4O_9) \times 2.25 \qquad (1.)$$

$$O/Ce = mol.\%(CeO_2) \times 2 + mol.\%(Ce_2O_3) \times 1.5 \qquad (2.)$$

$$O/(U+Ce) = (1-x_{Ce}) \times (O/U) + x_{Ce} \times (O/Ce) \qquad (3.)$$

EXAFS. Uranium U-L_3 EXAFS measurements were performed at European Synchrotron Radiation Facility (ESRF, Grenoble) on the HZDR-operated Rossendorf Beamline (BM20) [35]. EXAFS data were recorded at 15K using an He cryostat. A Si(111) double crystal-

8

monochromator coupled with collimating and focusing Rh-coated mirrors was used for the measurements. U-L$_3$ XAS data were recorded in the transmission mode using Ar/N$_2$ filled ionization chambers and in fluorescence mode with an electrically cooled (Cryo-Pulse 5 Plus) 18-element germanium detector (Ultra-LEGe, GUL0055, Mirion Technologies). The energy was calibrated using the Y K edge (17038 eV) of a Y metallic reference foil.

The EXAFS oscillations were fitted using the Artemis software included in the Demeter package [33]. Fourier transform was carried out on the k3-weighed data between 3.5 and 13.5 Å^{-1} using the Hanning function. The FT data were then fitted in the 1.5-4.7 Å window, by taking into account a three-shell model. This latter accounts for the first three distances, i.e. U-O(1) (which varies from 2.338 Å in CeO$_2$ to 2.372 Å in UO$_2$), U-M (3.83 – 3.87 Å) and U-O(2) (4.48 – 4.52 Å) [36]. The value of the amplitude reduction factor (S_0^2) was fixed to 0.92 [37]. Other parameters were obtained from the fit, including inner potential shift (ΔE_0), bond distances (d), Debye-Waller factors (σ^2), and coordination numbers. For this latter, exception was made for the third shell, where the ideal number (24) was fixed.

3. Results and discussion

3.1. Characterization of the starting powder

In a first step, the structure and the cationic homogeneity of the starting powders obtained after heating at 700°C under Ar/H$_2$ atmosphere for 4 hours were investigated. The PXRD patterns reported in **Figure 1** confirmed that all the samples presented the expected fluorite-type structure characteristic of U$_{1-x}$Ce$_x$O$_{2\pm\delta}$ solid solutions. Nevertheless, the associated unit cell parameters determined from Rietveld refinement appeared to be significantly lower than that expected from stoichiometric compounds with $\frac{O}{U+Ce}$ = 2.00 (**Table 2**). Indeed, if one considers the formation of an ideal solid solution, and the values reported in the literature for parent end-members (UO$_2$: a = 5.4713 Å [38]; CeO$_2$: a = 5.4097 Å [39]), the variation of the unit cell parameter (expressed in Å) versus x$_{Ce}$ should follow a linear trend with :

$$a = 5.4713 - 0.0616 \times x_{Ce} \tag{4.}$$

Such a deviation from the expected value could be correlated with the partial oxidization of U(IV) into U(V) or even U(VI) in the samples, as recently evidenced by Prieur *et al.* [26]. Indeed, despite the storage of the samples in an inert glovebox (O$_2$ < 0.1 ppm, i.e. P(O$_2$) < 10^{-2} Pa), their very high reactivity associated with their nanoscale size probably led to an oxidative ageing during PXRD sample preparation and/or measurement, both conducted under ambient air.
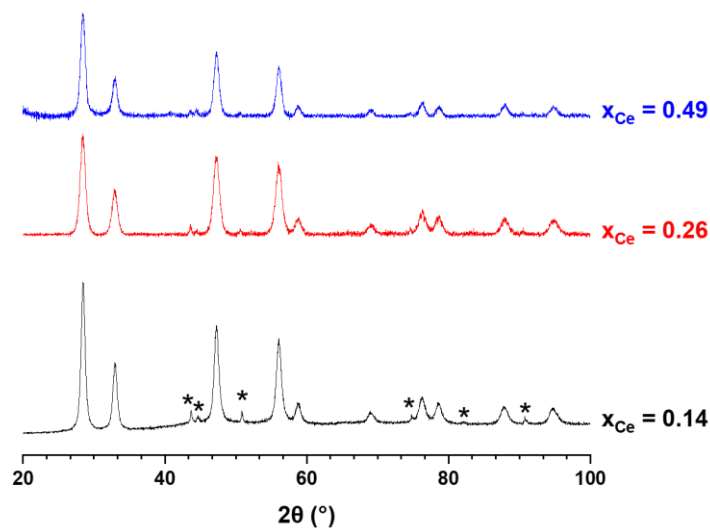
Figure 1. PXRD diagrams of $U_{1-x}Ce_xO_{2+\delta}$ powder samples after heat treatment at T = 700°C under Ar/H_2 atmosphere for 4 hours. The signal assigned to the sample holder (austenite with trace amounts of ferrite) is marked by *.

Table 2. Unit cell parameters and average crystallite size of the $U_{1-x}Ce_xO_{2+\delta}$ powder samples obtained after heat treatment at T = 700°C under Ar/H_2 atmosphere for 4 hours, coming from Rietveld refinement. The values obtained from the Vegard's law for stoichiometric compouds (O/(U+Ce) = 2.00) are supplied for comparison.

x_{Ce}	Unit cell parameter (Å)		Average crystallite size (nm)
	Vegard's law	*PXRD*	
0.14	5.4627	5.4571(1)	17(1)
0.26	5.4553	5.4390(3)	8(1)
0.49	5.4411	5.4389(3)	8(1)

Additionally, SEM and EDS investigations were conducted to point out the morphology of the powders and to study their homogeneity in terms of cationic distribution. The results obtained for x_{Ce} = 0.26 are presented as an example in **Figure 2**, with similar features being obtained for all the chemical compositions studied. SEM observations confirmed that the powder samples consisted of nanoscale crystallites assembled as micrometric aggregates, in good agreement with PXRD results. The agglomeration of the elementary crystallites most likely resulted from heating at 700°C. Nevertheless, it did not promote a strong grain growth, since the average crystallite size remained typically close to 10 nm. Hence, the reactivity of the powders towards densification was preserved, with specific surface areas typically between 10 and 30 $m^2.g^{-1}$ [21].

The statistical distribution of the U and Ce cations within the powder samples was then studied by EDS analyses. From **Figure 2**, it can be seen that the distribution of the $\frac{Ce}{U+Ce}$ molar ratio, illustrating the chemical composition of the sample, follows a Gaussian law. Although not strictly identical, the value of the centroid (x_{Ce} = 0.232) matches the expected value and that coming from ICP-AES analysis, the slight differences being assigned to the conditions of acquisition that preclude a fully quantitative analysis. More importantly, the standard deviation around the average x_{Ce} value appeared to be very limited (σ = 0.012). As such, 95% of the datapoints are located within a range 0.208 < x_{Ce} < 0.256. Comparable results were obtained for the other composition studied, and are supplied as supplementary information (**Figure S1**). Hence, no U- or Ce- hot-spots were detected, contrarily to the typical microstructures of samples prepared by powder metallurgy processes, i.e. mixture of oxide

powders [40]. This sample series can also be considered to be more homogeneous than some other oxide compounds prepared from the initial precipitation of low-temperature precursors [41], in which the presence of large amounts of cerium in the starting mixture could lead to polyphasic systems [42].

From these results, the powder samples prepared during this work appear to be highly homogenous, and are expected to be strongly reactive towards sintering due to their nanometric grain size. As such, they ensure the rapid diffusion of oxygen atoms and cations during the heat treatments performed at high temperature, thus the preparation of sintered samples at the thermodynamic equilibrium.
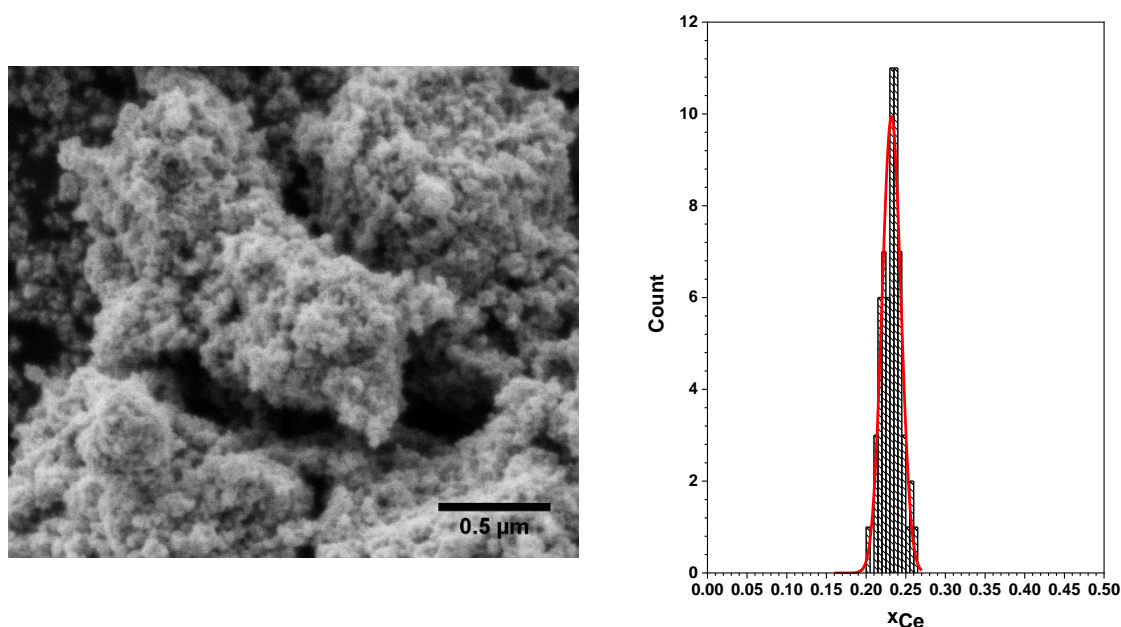

Figure 2.   SEM micrograph of $U_{0.74}Ce_{0.26}O_{2+\delta}$ sample after heat treatment at T = 700°C under Ar/H_2 atmosphere for 4 hours (left) and statistical distribution of the x_{Ce} = Ce/(U+Ce) molar ratio determined by EDS analyses (right).

3.2. HERFD-XANES

Representative selection of HERFD-XANES spectra recorded at U-M_4 and Ce-L_3 edges for the various $U_{1-x}Ce_xO_{2+\delta}$ sintered samples studied, as well as spectra of references are compiled in **Figure 3**. The spectra collected for the other samples are supplied as supporting information (**Figure S2**). As demonstrated in previous works [33, 43, 44], HERFD-XANES provides a remarkable resolution in energy that allows the separation of the characteristic

12

peaks of U(IV), U(V) and U(VI), and gives an accurate insight on the redox speciation of uranium. As such, the spectrum of UO_2 only presents one large peak assigned to U(IV) at around 3725 eV, while that of U_4O_9 exhibits two peaks with comparable intensities corresponding to U(IV) and U(V) contributions, this latter around 3726 eV. Comparatively, the spectrum associated to U_3O_8 usually shows a large signal located around 3727 eV that accounted for U(V) and U(VI) (not shown here).
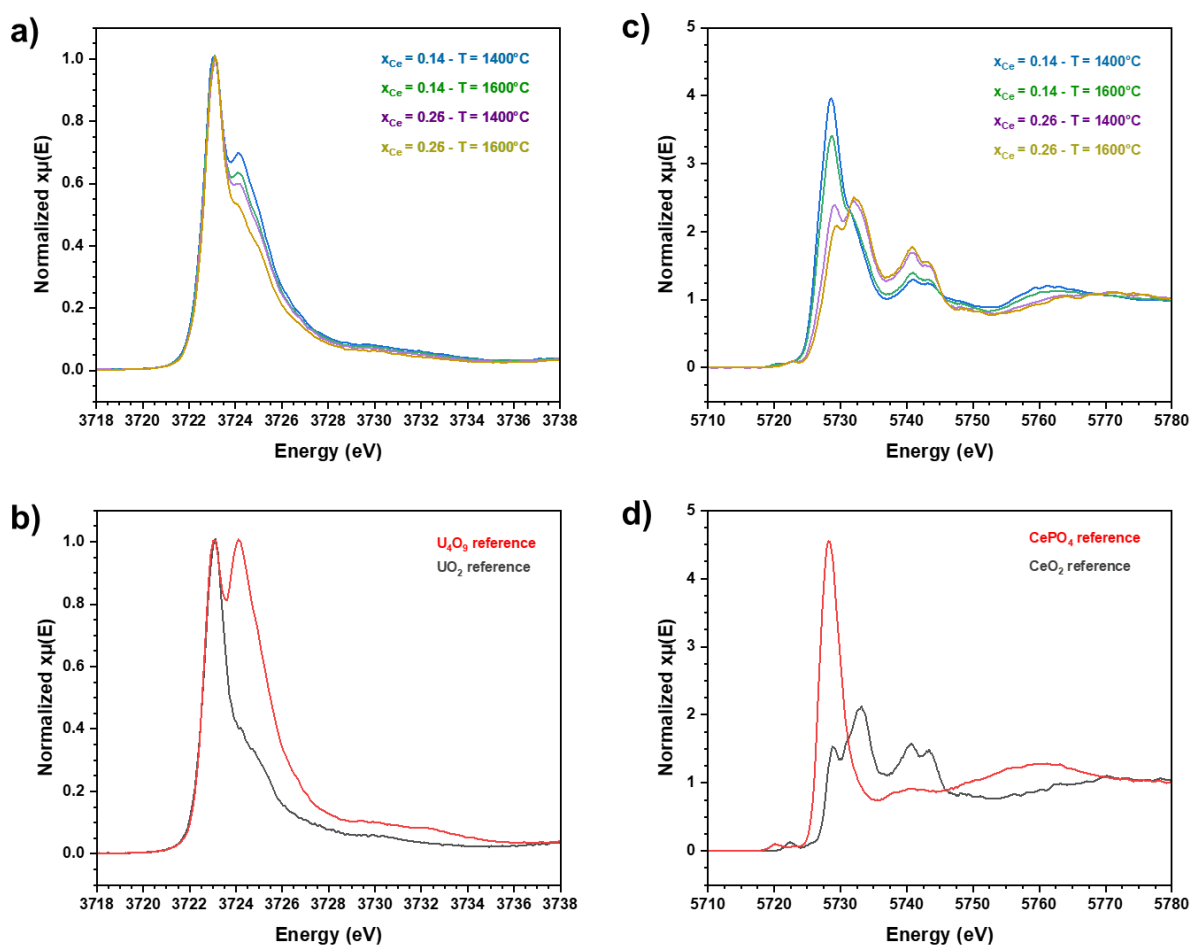

Figure 3.   Normalized HERFD-XANES spectra at the U-M_4 (a – samples; b - references) and Ce-L_3 (c – samples; d - references) edges for various $U_{1-x}Ce_xO_{2+\delta}$ samples sintered under argon atmosphere.

The spectra recorded from the different $U_{1-x}Ce_xO_{2+\delta}$ sintered samples prepared are typically comprised between those of UO_2 and U_4O_9, meaning that they mainly consist of U(IV) with variable amounts of U(V). In order to quantify the proportion of the different oxidation states of uranium within the samples, HERFD-XANES spectra were fitted through a linear combination of reference spectra. In these latter, we assumed that $UO_{2.00}$ was completely

composed of U(IV), U_4O_9 was in a ratio U(IV):U(V) = 1:1, and that U(V):U(VI) = 2:1 in U_3O_8. From these values and the contribution of each reference spectra, the average oxidation state of uranium was determined and gathered in **Table 3** while **Figure 4** presents the fit results obtained for the $U_{0.74}Ce_{0.26}O_{2+\delta}$ sample sintered at T = 1600°C under Ar atmosphere. For all the samples studied, the quality factor X^2 remained below 0.04.

All the results evidenced the absence of U(VI) traces in our samples, which notably differs from the findings of Prieur *et al.* [26], who systematically detected variable amounts of U(VI) in nanocrystalline $U_{1-x}Ce_xO_{2+\delta}$, mainly due to the physical form of their samples and their preparation route, i.e. hydrothermal conversion (T = 200°C, t = 4 hours) of mixed hydroxide under aerated conditions. In our study, sintering at high temperature promotes the reduction of U(VI) into U(V) or even U(IV), depending on the sintering atmosphere considered (i.e. the oxygen partial pressure). As such, samples sintered under argon include variable amounts of U(V), that are ranging from 5 to 35% depending on the sintering temperature.
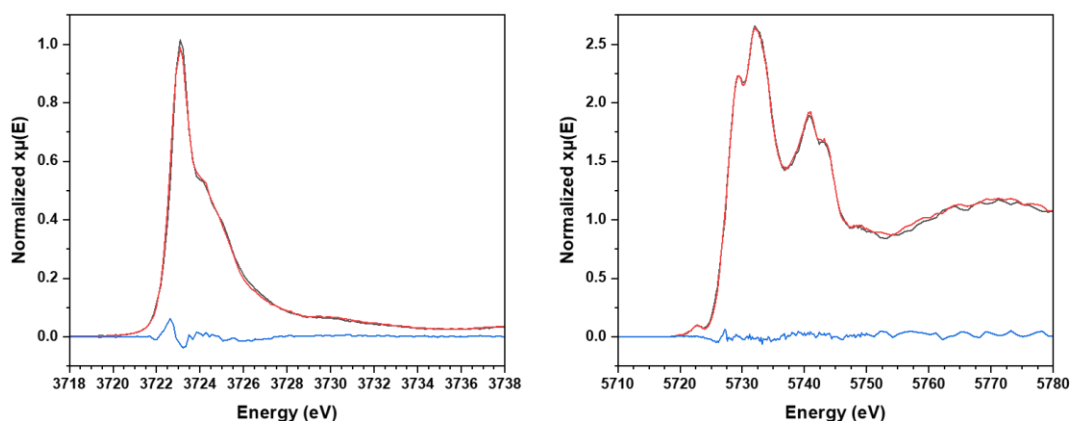

Figure 4.   Observed (black), calculated (red) and difference (blue) HERFD-XANES spectra at the U-M_4 (left) and Ce-L_3 (right) edges for $U_{0.74}Ce_{0.26}O_{2+\delta}$ sintered at T = 1600°C under Ar atmosphere.

Conversely, all the samples densified under reducing Ar/H_2 mixture led only to a very small proportion of U(V), systematically close to 5%. Owing to the atmosphere chosen, which is expected to yield a complete reduction of uranium into U(IV), this value is likely to reflect a slight reoxidation of the samples after the heat treatment. This latter could occur right after pulling the pellets out of the furnace, *i.e.* when exposing them to ambient air, and/or during the preparation of the XAS samples, which required mechanical crushing of the pellets. In

14

both cases, uranium was probably oxidized at the extreme surface of the solids, thus explaining the small fraction of U(V) measured herein.

Compared to uranium, the signal recorded at the L_3-edge of cerium appeared to be much more complex. Particularly, CeO_2 is characterized by three distinct features: a pre-edge peak (5722 eV), as well as two doublets at around 5729/5733 and 5741/5743 eV, originating from 2p3/2 $\rightarrow$ 5d5/2 transitions. On the other hand, the spectrum of $CePO_4$ monazite, which comprises pure Ce(III) [45], only presents one characteristic large peak, centered at around 5728 eV. As for uranium, the data associated to the different $U_{1-x}Ce_xO_{2+\delta}$ sintered samples mostly depends on the atmosphere chosen for the heat treatment at high temperature. Surprisingly, the proportion of Ce(III) remained negligible under reducing atmosphere, while it varied from 9 up to 67 % under argon.

Table 3. Contribution of the different species to the average oxidation state (OS) of uranium and cerium, as determined from linear combination fitting of HERFD-XANES data. The numbers between parentheses indicate the uncertainty on the last digit.

x_{Ce}	Sintering conditions	Atm.	U(IV)	U(V)	U OS	Ce(III)	Ce(IV)	Ce OS
0.14	1400°C – 10h	Ar/H₂	94 (1)	6 (1)	4.06	3 (2)	97 (2)	3.97
	1600°C – 0h	Ar/H₂	96 (1)	4 (1)	4.04	0 (2)	100 (2)	4.00
0.26	1300°C – 10h	Ar/H₂	93 (1)	7 (1)	4.07	2 (2)	98 (2)	3.98
	1400°C – 10h	Ar/H₂	94 (1)	6 (1)	4.06	1 (2)	99 (2)	3.99
	1500°C – 10h	Ar/H₂	94 (1)	6 (1)	4.06	0 (2)	100 (2)	4.00
	1600°C – 0h	Ar/H₂	95 (1)	5 (1)	4.05	0 (2)	100 (2)	4.00
0.49	1400°C – 10h	Ar/H₂	96 (1)	4 (1)	4.04	0 (2)	100 (2)	4.00
	1600°C – 0h	Ar/H₂	95 (1)	5 (1)	4.05	0 (2)	100 (2)	4.00
0.14	1400°C – 10h	Ar	74 (1)	26 (1)	4.26	67 (2)	33 (2)	3.32
	1600°C – 0h	Ar	80 (1)	20 (1)	4.20	54 (2)	46 (2)	3.45
0.26	1300°C – 10h	Ar	65 (1)	35 (1)	4.35	46 (2)	54 (2)	3.54
	1400°C – 10h	Ar	82 (1)	18 (1)	4.18	21 (2)	79 (2)	3.79
	1500°C – 10h	Ar	94 (1)	6 (1)	4.06	0 (2)	100 (2)	4.00
	1600°C – 0h	Ar	89 (1)	11 (1)	4.11	9 (2)	91 (2)	3.91

| 0.49 | 1400°C – 10h | Ar | 94 (1) | 6 (1) | 4.06 | 0 (2) | 100 (5) | 4.00 |
| | 1600°C – 0h | Ar | 96 (1) | 4 (1) | 4.04 | 0 (2) | 100 (5) | 4.00 |

Such results show that in the range of composition covered by this study, the redox speciation of the cations is mainly governed by the behavior of uranium. Indeed, under reducing Ar/H$_2$ atmosphere, all the samples mostly contain U(IV), as expected from the behavior of pure UO$_2$. More surprisingly, cerium is also fully tetravalent, while CeO$_2$ would turned into Ce$_2$O$_3$ almost completely in similar conditions [46]. As such, tetravalent uranium appears to have a protective effect over the reduction of Ce(IV) into Ce(III), resulting in stoichiometric samples with O/M close to 2.00 (**Table 4**).

Table 4.   Determination of O/U, O/Ce and O/M molar ratios in the various samples investigated from the linear combination fitting of HERFD-XANES data.

x_{Ce}	**Sintering conditions**	**O/U**		**O/Ce**		**O/M**	
		Ar/H$_2$	Ar	Ar/H$_2$	Ar	Ar/H$_2$	Ar
0.14	1400°C – 10h	2.03	2.13	1.98	1.66	2.02	2.06
	1600°C – 0h	2.02	2.10	2.00	1.73	2.02	2.05
0.26	1300°C – 10h	2.03	2.17	1.99	1.77	2.02	2.06
	1400°C – 10h	2.03	2.09	1.99	1.90	2.02	2.04
	1500°C – 10h	2.03	2.03	2.00	2.00	2.02	2.02
	1600°C – 0h	2.03	2.05	2.00	1.96	2.02	2.03
0.49	1400°C – 10h	2.02	2.03	2.00	2.00	2.01	2.02
	1600°C – 0h	2.03	2.02	2.00	2.00	2.02	2.01

Under argon, the increase of the partial pressure in oxygen led U(IV) to oxidize into U(V). Correlatively, Ce(IV) was reduced to counter-balance the charge, in good agreement with the compensation mechanisms reported in the literature for several UO$_2$-Ln$_2$O$_3$ systems [25, 47]. Indeed, the incorporation of trivalent rare earth elements in the fluorite-type structure of UO$_2$ is balanced by the partial oxidization of U(IV) into U(V), although with a small fraction of oxygen vacancies [25]. Nevertheless, it is important to note that the U(V)-Ce(III) compensation

was never complete, still resulting in hyper-stoichiometric samples. This feature, which could appear to be counter intuitive, was already observed for $(U,Pu)O_2$ mixed oxides [48]. Also, it is important to note that the fraction of U(V), and correlatively that of Ce(III), varies with both the sintering temperature and the total amount of cerium incorporated in the sample (**Figure 5**).
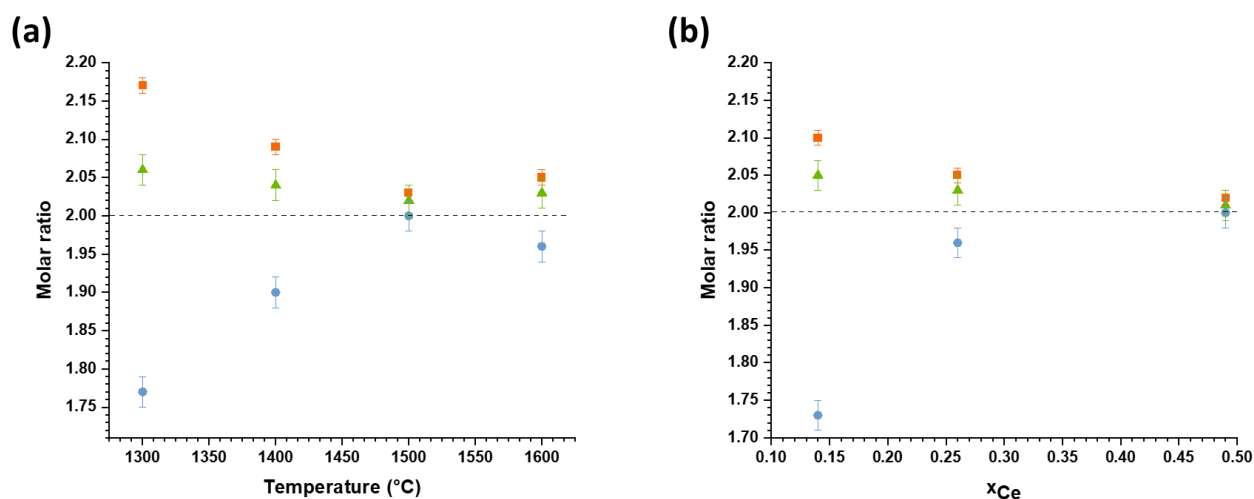
Figure 5. Variation of the O/U (■), O/Ce (●) and O/M (▲) molar ratios under argon atmosphere as a function of (a) the sintering temperature ($x_{Ce} = 0.26$) and of (b) the chemical composition (T = 1600°C).

Indeed, the samples sintered at low-temperature (typically 1300-1400°C) appeared to be clearly hyper-stoichiometric, with O/M ratios close to 2.05 and beyond. Conversely, sintering above 1500°C systematically led to O/M close to 2.00, even if the sample prepared at 1600°C slightly deviates from this trend due to the difference in holding time (cf. experimental section). With a similar trend, the stoichiometry of the samples came close to 2.00 when the amount of cerium incorporated increased. As such, all the samples prepared with $x_{Ce} = 0.49$ were found to be almost stoichiometric whatever the conditions selected. These tendencies are in good agreement with the results presented by Markin *et al.* in the U-Ce-O ternary phase diagram. Indeed, these authors stated that the $MO_{2+y} + M_4O_{9-\delta}$ domain was reduced to the benefit of single phase MO_{2+y} when increasing the temperature and the cerium content [49].

3.4. EXAFS at the U-L$_3$ edge

As HERFD-XANES showed that the most important impact on the samples' stoichiometry was obtained when varying the sintering temperature from 1300°C to 1600°C under argon, a complementary EXAFS study was conducted to investigate the local environment of the uranium cation in these samples. The comparison of the U-L_3 EXAFS spectra plotted in the R-space for all the x = 0.26 samples sintered under argon atmosphere is provided in **Figure 6**. The pseudo radial distribution function (RDF) modulus systematically exhibited the same features, with a first peak close to 2 Å corresponding to the apparent distance of the first shell U−O(1), and a second one located around 3.8 Å, mainly due to the U−U interactions, with a small contribution of the U−O(2) shell. The spectra mostly differ from the magnitude of the RDF, which is mainly linked to the coordination numbers and/or to the structural disorder. As such, the increase of the intensity with the sintering temperature could be linked both with the evolution of the O/M ratio towards the ideal 2.00 value, as well as to the grain growth phenomena associated with sintering, which promotes the expansion of the coherent domain lengths, resulting in an improved crystallinity. Accordingly, the coordination number on the first shell increases with the sintering temperature, but remains below the theoretical value of 8 for uranium in the $UO_{2.00}$ structure: this defect is thus directly linked with the presence of Ce(III) in the samples, that lower the oxygen content in the solid.

The RDF assigned to the pellet sintered under argon at 1300°C, which exhibits the highest O/M ratio determined in this work (O/M = 2.06), appeared to be shifted towards lower apparent distances. This feature is in good agreement with an oxidized sample, which is usually assigned to a smaller unit cell volume (see the XRD section hereafter), and then to shorter U-O(1) bond lengths (**Table 5**). Still, the distance measured for this sample (d = 2.343(4) Å) is only 1% smaller than the value reported by Martin et al. [36] for a stoichiometric sample (O/M = 2.00), although with a slightly different cerium content (x_{Ce} = 0.25). Even if hyper-stoichiometry was found to generate a limited contraction of the first coordination shell, distortion effects were still evidenced by higher Debye−Waller factors. Indeed, these latter directly account for structural disorder, as the thermic agitation could be considered to be negligible for measurements performed at 15K. Conversely to the first coordination layer, the second and third shells were less impacted, as the U-U and U-O(2) distances remained close to 3.84 and 4.48 Å, respectively, for all the sintering temperatures considered.

The data extracted from the EXAFS spectra of $U_{0.74}Ce_{0.26}O_{2+\delta}$ sintered samples under reducing Ar/H_2 atmosphere led to less significative variations, once again in good agreement with the results coming from HERFD-XANES, as their O/M stoichiometry was

systematically found close to 2.00. Hence, on the one hand, neither interatomic distances nor Debye-Weller factors were found to vary significantly, except for the sample sintered at 1600°C, probably due to the absence of an isothermal plateau at the targeted temperature. On this basis, U-O(1), U-U, and U-O(2) distances appeared in very good agreement with the data reported by Martin *et al.* [36] for stoichiometric samples, owing to the uncertainties attached with both measurements series. On the other hand, the coordination number for the first two shells (U-O(1) and U-U) was found to increase slightly but continuously from 1300°C to 1600°C, even if this variation remains in the same order of magnitude than the uncertainties attached with the measurement. This probably stemmed from the grain growth occurring during the sintering process, which enhanced the contribution of bulk versus surface. Indeed, nanometric grain size are generally associated to the predominance of surface species that are characterized by incomplete coordination layer, thus decreasing the global N value [50].

Table 5. Best fit results for the first three coordination shells at the uranium L_3 edge. The numbers between parentheses indicate the uncertainty on the last digit.

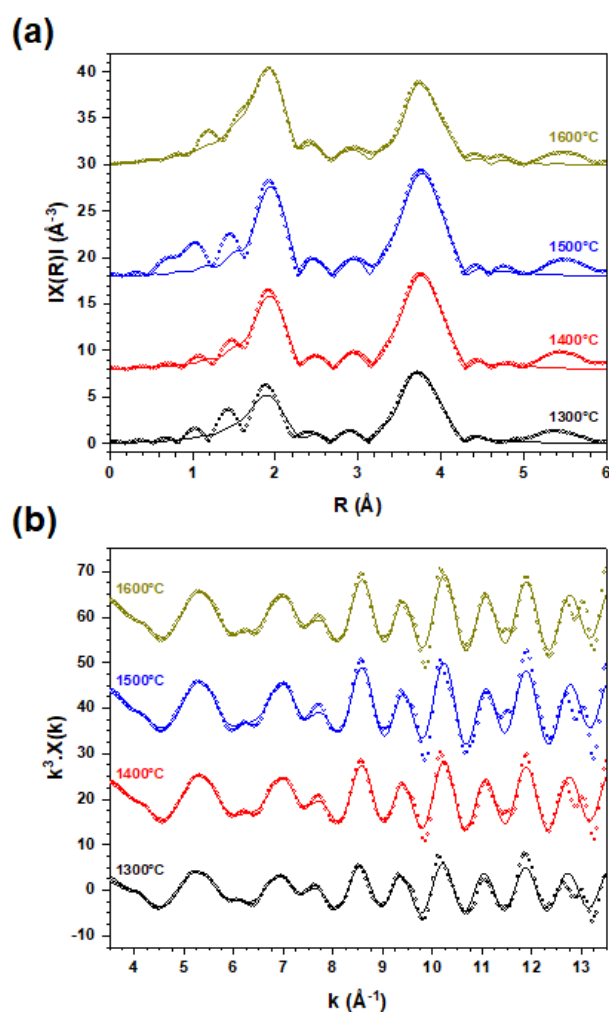| Sintering	Atm.	First shell : U-O$_{(1)}$			Second shell : U-U			Third shell : U-O$_{(2)}$	
		d (Å)	N	σ^2 $(10^3 \times \text{Å}^2)$	d (Å)	N	σ^2 $(10^3 \times \text{Å}^2)$	d (Å)	σ^2 $(10^3 \times \text{Å}^2)$
1300°C-10h	Ar	2.343(4)	6.9(5)	8.2(7)	3.846(3)	9.5(6)	4.8(4)	4.49(1)	10(2)
1400°C-10h	Ar	2.360(3)	7.5(5)	5.3(5)	3.846(2)	10.6(5)	4.1(3)	4.48(1)	8(2)
1500°C-10h	Ar	2.366(4)	7.4(5)	3.6(6)	3.840(3)	11.3(7)	4.0(3)	4.48(1)	7(2)
1600°C-0h	Ar	2.356(3)	7.5(5)	4.4(5)	3.834(3)	11.1(6)	4.1(3)	4.47(1)	7(1)
1300°C-10h	Ar/H$_2$ 4%	2.369(5)	7.5(5)	3.8(8)	3.844(5)	11.0(9)	4.0(4)	4.49(2)	7(3)
1400°C-10h	Ar/H$_2$ 4%	2.366(4)	7.8(5)	4.2(6)	3.843(3)	11.4(7)	4.0(2)	4.48(1)	6(2)
1500°C-10h	Ar/H$_2$ 4%	2.367(4)	7.9(5)	4.1(7)	3.842(3)	11.6(7)	4.0(3)	4.48(1)	6(2)
1600°C-0h	Ar/H$_2$ 4%	2.356(2)	8.0(5)	4.3(4)	3.864(2)	11.8(4)	2.6(2)	4.491(7)	5(1)
Reference									
Martin *et al.*,		2.362(8)	8.0(2)	6.2(6)	3.857(9)	9.0(5)	4.2(4)	4.51(4)	9(2)

Figure 6. Uranium L$_3$-edge k^3-weighed EXAFS data (b) and Fourier transform (a) for U$_{0.74}$Ce$_{0.26}$O$_{2+\delta}$ samples sintered under Ar at 1300°C (black), 1400°C (red), 1500°C (blue) and 1600°C (mustard), including best fits (solid lines). The FT window was taken over the k-space range from 3.5 to 13.5 Å^{-1} and magnified by k^3.

3.5. X-Ray Diffraction

As explained in the introduction, the structure of uranium-cerium dioxide solid solutions has been widely explored in the literature, involving both stoichiometric, hyper-stoichiometric and sub-stoichiometric samples regarding oxygen. A large domain of chemical compositions has also been assessed, that goes from pure UO$_2$ containing some mol.% in cerium, to highly Ce-enriched samples. Different sets of unit cell parameters coming from these studies have

been compiled in **Figure 7** to give an overview of the impact of Ce content and O/M ratio on the structure of $U_{1-x}Ce_xO_{2\pm\delta}$ mixed oxides.

Even if a precise measurement of the O/M stoichiometry was frequently neglected by the various authors, most of the results reported for stoichiometric samples are distributed on a straight-line accounting for the Vegard's law (**Figure 7b**). Nevertheless, one can observe that almost all the datapoints lie slightly below the theoretical line drawn from pure UO_2 and CeO_2 data, meaning that the samples analyzed probably presented a slight deviation from the ideal O/M = 2.00 stoichiometry. This feature could be explained by the very high tendency of U(IV) to oxidize in air, that has been observed in the present study when dealing with samples sintered under reducing Ar-H_2 atmosphere, and which is even more strengthened when dealing with powders.

Overall, the sub-stoichiometric domain was scarcely investigated, probably due to the difficulty to obtain such samples. This fits well with the results obtained from the HERFD-XANES study performed in this work, where even reducing conditions produced stoichiometric samples composed of U(IV) and Ce(IV). When O/M ratio below 2.00 was reached, the value of the unit cell parameter increased in regards of the Vegard's law. This tendency was explained by the presence of significant amounts of Ce(III), and by the formation of oxygen vacancies to counterbalance the charge defect. Nevertheless, while the values published by Tagawa *et al.* remained close to the Vegard's law [51], those from Lorenzelli appeared to be strongly different and might probably be considered with caution [52] (**Figure 7a**). Also, it is important to note that when the amount of cerium incorporated in the samples increased (typically $x_{Ce} > 0.60$), the unit cell parameter got closer to the Vegard's law, indicating almost negligible deviation from the stoichiometry despite the conditions applied.

In the hyper-stoichiometric domain (**Figure 7c**), the deviation from O/M = 2.00 is accompanied by the decrease of the unit cell parameter, in good agreement with what is generally observed for UO_{2+x} samples [43]. This tendency is particularly marked for samples enriched in uranium for which Nawada *et al.* have reported samples with O/M molar ratio as high as 2.28 [53]. However, as detailed previously, all the compounds with $x_{Ce} > 0.60$ almost fit with the Vegard's law. Hence, cerium-enriched $U_{1-x}Ce_xO_{2+\delta}$ solid solutions appear to be weakly impacted by both the physical form of the sample and the operating conditions (temperature, atmosphere) that all lead to stoichiometric samples.
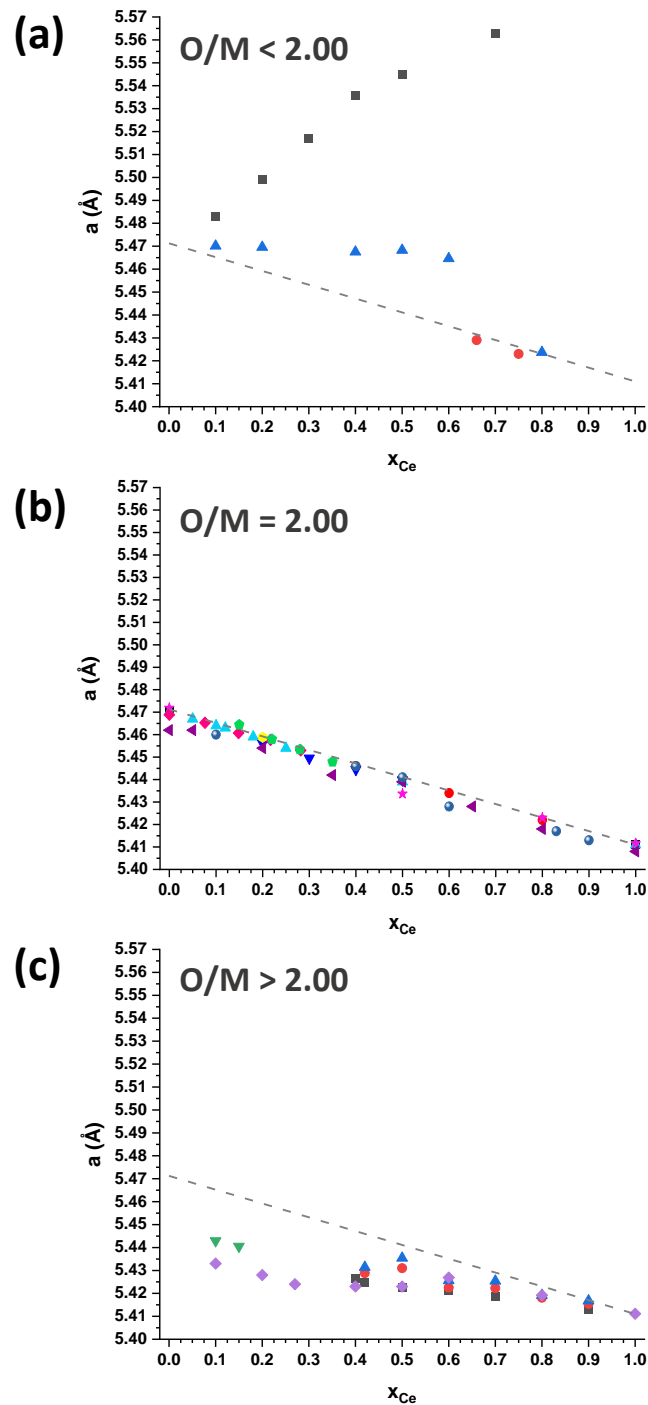
Figure 7. Variation of the unit cell parameters of $U_{1-x}Ce_xO_{2\pm\delta}$ reported in the literature for (a) sub-stoichiometric samples with O/M < 2.00 - ■ : Lorenzelli *et al.* [52]; ▲ : Tagawa *et al.* [51] ● : Markin *et al.* [49]; (b) stoichiometric samples with O/M = 2.00 - ■: Dörr *et al.* [54]; ● : Krishnan *et al.* [20]; ▲ : Martin *et al.* [36]; ★ : Krishnan *et al.* [55]; ▼ - Nagarajan *et al.* [56]; ◆ : Kim *et al.* [57]; ◀ : Cao *et al.* [58]; ▶ : Markin *et al.* [49]; ⬠ : Kurosaki *et al.* [59]; ⬠ : Designan *et al.* [13]; ⊙ : Prieur *et al.* [60]; ⊙ : Zinkevich *et al.* [61]; (c) hyper-stoichiometric samples with O/M > 2.00 – Nawada *et al.* [53] ■ (873 K), ● (1123 K), ▲ (1273 K); ▼ : Markin *et al.* [49]; ◆ : Tagawa *et al.* [51]. The dashed lined represents the Vegard's law extrapolated from pure UO_2 [38] and CeO_2 [26] data.

The results obtained in this study, either by laboratory PXRD or by Synchrotron measurements, confirm the trends presented above. The unit cell parameters obtained by Rietveld refinement are gathered in **Table 6**, while an example of fit is supplied for each technique as supplementaty information (**Figure S3**). Confidence parameters attached to the Rietveld refinements are also supplied as supplementary information in **Tables S1 and S2**. Both series of values are consistent with each other, even if the unit cell parameters determined by PXRD generally stand slightly above those obtained by S-PXRD. This small discrepancy might originate from the differences in the experimental setups, but also from the preparation schedule of the samples. Indeed, laboratory PXRD were generally performed shorty after the fabrication of the samples, while these latter were stored for several weeks prior to synchrotron measurements, probably leading to a limited oxidation of uranium at the surface.

Table 6.   Unit cell parameter of the $U_{1-x}Ce_xO_{2+\delta}$ sintered samples (expressed in Å), as determined by Rietveld refinement of PXRD and S-PXRD data.

x_{Ce}	Sintering conditions	PXRD		S-PXRD	
		Ar/H_2	Ar	Ar/H_2	Ar
0.14	1400°C – 10h	5.4649(1)	5.4591(1)	5.4620(1)	5.4567(1)
	1600°C – 0h	5.4648(1)	5.4603(1)	5.4624(1)	5.4584(1)
0.26	1300°C – 10h	5.4549(1)	5.4537(1)	5.4532(1)	5.4519(1)
	1400°C – 10h	5.4557(1)	5.4554(1)	5.4528(1)	5.4519(1)
	1500°C – 10h	5.4548(1)	5.4547(1)	5.4524(1)	5.4528(1)
	1600°C – 0h	5.4550(1)	5.4543(1)	5.4529(1)	5.4519(1)
0.49	1400°C – 10h	5.4408(1)	5.4407(1)	5.4378(1)	5.4380(1)
	1600°C – 0h	5.4434(1)	5.4420(1)	5.4385(1)	5.4378(1)

The impact of the O/M ratio and of the cerium content on the structure of $U_{1-x}Ce_xO_{2+\delta}$ solid solutions was further evaluated by plotting the variation of the unit cell parameter of several samples as a function of the deviation from the O/M = 2.00 stoichiometry (**Figure 8**). In this aim, only S-PXRD results were considered for a matter of consistency, as O/M ratios were determined from synchrotron measurements.

Within the oxygen stoichiometry range addressed (*i.e.* $2.01 \leq O/M \leq 2.06$), only slight variations of the unit cell parameter were observed, that were typically about 0.1% of the value calculated for the stoichiometric samples from equation (4.). Also, although the unit cell parameter decreases linearly versus δ for $x_{Ce} = 0.14$, no clear trend can be deduced from the datapoints obtained for higher cerium contents. In order to go further, the structural data collected in this work was then compared to the relation reported by Sali *et al.* [62], which links the unit cell parameter (a, expressed in Å), the chemical composition (x_{Ce}) and the deviation from the stoichiometry (δ) such as:

$$a = 5.4704 - 0.060 \times x_{Ce} - 0.07 \times \delta \qquad (5.)$$

This equation was given only for $0.21 < x_{Ce} < 0.44$, which remains close to the compositon range studied herein. The comparison between the two datasets shows a reasonable agreement, as evidenced in **Figure 8**. Indeed, in most of the cases, evaluating the O/M ratio from the interpolation of our S-PXRD results with Sali's relation would lead to an absolute error of about 0.02 or less, which is typically in the same order of magnitude than that coming from other experimental techniques such as TGA. As in the case of the Duriez relationship established for $U_{1-x}Pu_xO_{2+\delta}$ solid solutions [63], equation (5.) then might be used as a first approximation to estimate simply the O/M stoichiometry of uranium-cerium mixed oxides, knowing their composition and their structural features.
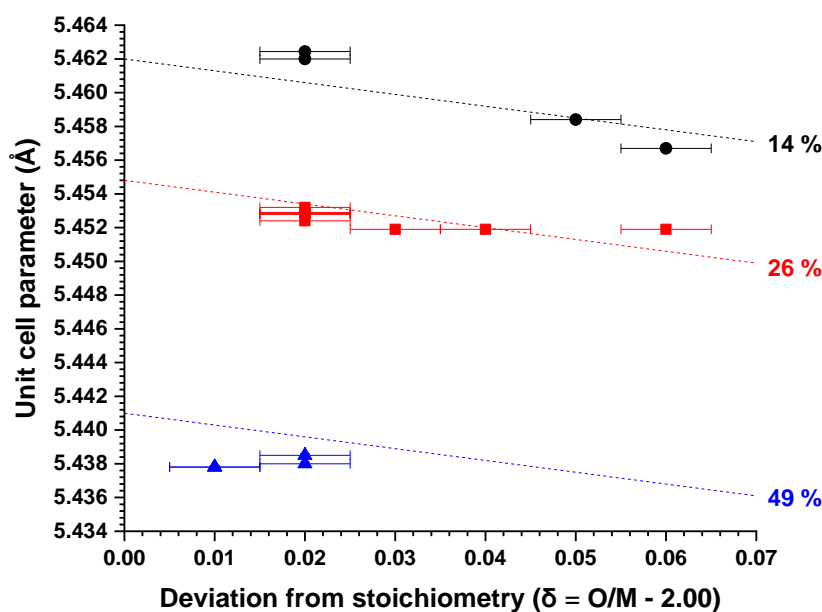
Figure 8. Variation of the unit cell parameters of $U_{1-x}Ce_xO_{2+\delta}$ samples prepared in this work as a function of the deviation from stoichiometry. The dotted lines account for the relation proposed by Sali *et al.* [62].

4. Conclusion

In this work, the use of nanometric and highly reactive uranium-cerium dioxide powders prepared by wet-chemistry route led to the fabrication of homogenous and dense $U_{1-x}Ce_xO_{2+\delta}$ solid solutions after sintering at high temperature. As such, these samples allowed to study thoroughly the impact of the operating conditions chosen for the heat treatment (firing temperature, oxygen partial pressure), on the structure and redox speciation of the final ceramics.

For this latter, HERFD-XANES spectroscopy led to determine accurately the oxygen / metal molar ratios (*i.e.* O/M with M = U + Ce) in all the samples prepared. Under reducing atmosphere ($PO_2 \sim 6{\times}10^{-29}$ atm), the oxides were found to be close to O/M = 2.00. Even if a limited fraction of the uranium (typically 5% or less) was found to be oxidized as U(V), it was more likely to arise from the storage and the preparation of the samples for synchrotron measurements. Hence, one can consider that in the furnace, the dioxide compounds were stoichiometric, with U(IV) preventing cerium from the reduction into Ce(III). Conversely, the O/M ratio in the samples prepared under argon ($PO_2 \sim 2{\times}10^{-6}$ atm) varied with the sintering conditions. They globally appeared to be hyper-stoichiometric (*i.e.* O/M > 2.00), the departure from the dioxide stoichiometry decreasing with both the cerium content in the sample, and the sintering temperature. The reduction of the Ce(IV) present in the precursor into Ce(III) was then not sufficient to counter-balance the oxidation of U(IV) into U(V) under the operating conditions chosen. Nevertheless, such deviation from the ideal O/M = 2.00 ratio was found to generate only moderate structural disorder from EXAFS data at the U-L$_3$ edge, mainly in the first shell of coordination of the cations.

Indeed, whatever the sintering temperature and atmosphere, all the samples retained the fluorite-type structure of the UO_2 and CeO_2 end-members. The determination of accurate lattice parameters thanks to S-PXRD measurements led to complement the data already reported in the literature by various authors. These results were also consistent with the mathematic expression proposed by Sali *et al.* to link the unit cell parameter, the chemical composition and the deviation from the stoichiometry. The fair agreement observed confirms

25

that this relation can be used as a first approximation to estimate simply the O/M stoichiometry in uranium-cerium mixed oxides, typically within a ± 0.02 uncertainty.

The structural data reported herein then constitute a starting point for the evaluation of the impact of the O/M stoichiometry on several characteristics of dense uranium-cerium dioxide pellets, such as microstructure and chemical durability.

Associated Content

Supporting Information Available:

- Statistical distribution of the Ce/(U+Ce) ratio for x_{Ce} = 0.14 and x_{Ce} = 0.49 sample
- Normalized HERFD-XANES spectra at the U-M_4 and Ce-L_3 edges
- Example of PXRD and SPXRD patterns refined by the Rietveld method
- Unit cell parameters and confidence parameters obtained after the Rietveld refinement of PXRD and SPXRD

The Supporting Information is available free of charge on the ACS Publications website.

References

1. Kelly, J. E.: Generation IV International Forum: A decade of progress through international cooperation, *Prog Nucl Energ* **2014,** *77*, 240-246.
2. Poinssot, C.; Boullis, B.: Actinide recycling within closed fuel cycles, *Nucl Eng Int* **2012,** *57*, 17-21.
3. Courtin, F.; Laguerre, C.; Miranda, P.; Chabert, C.; Martin, G.: Pu multi-recycling scenarios towards a PWR fleet for a stabilization of spent fuel inventories in France, *Epj Nucl Sci Technol* **2021,** *7*.
4. Shabbir, M.; Robins, R. G.: Kinetics of Dissolution of Uranium Dioxide in Nitric Acid .I., *J Appl Chem* **1968,** *18*, 129-134.
5. Gonzalez, M. G.; Ponzi, E. N.; Laborde, M. A.; Lemcoff, N. O.: Dissolution of Uranium-Dioxide Pellets in Nitric-Acid, *Rev Lat Am Ing Quim* **1983,** *13*, 59-70.
6. Bruno, J.; Casas, I.; Cera, E.; Depablo, J.; Gimenez, J.; Torrero, M. E.: Uranium(Iv) Dioxide and Simfuel as Chemical Analogues of Nuclear Spent Fuel Matrix

Dissolution - a Comparison of Dissolution Results in a Standard NaCl/NaHCO$_3$ Solution, *Scientific Basis for Nuclear Waste Management XVIII* **1995**, *353*, 601-608.

7. Marc, P.; Magnaldo, A.; Vaudano, A.; Delahaye, T.; Schaer, E.: Dissolution of uranium dioxide in nitric acid media: what do we know?, *Epj Nucl Sci Technol* **2017**, *3*.

8. Ikeda, Y.; Yasuike, Y.; Nishimura, K.; Hasegawa, S.; Takashima, Y.: Kinetic-Study on Dissolution of UO$_2$ Powders in Nitric-Acid, *J Nucl Mater* **1995**, *224*, 266-272.

9. King, F.; Kolar, M.; Shoesmith, D. W.: Modelling the oxidative dissolution of UO$_2$, *Scientific Basis for Nuclear Waste Management XXII* **1999**, *556*, 463-470.

10. Pierce, E. M.; Martin, W. J.; Serne, R. J.; Icenhower, J. P.: Dissolution kinetics of UO$_2$ (cr), *Geochim Cosmochim Ac* **2002**, *66*, A602-A602.

11. Bertolotto, S.; Szenknect, S.; Lalleman, S.; Magnaldo, A.; Raison, P.; Odorico, M.; Podor, R.; Claparede, L.; Dacheux, N.: Effect of surface orientation on dissolution rate and surface dynamics of UO$_2$ single crystals in nitric acid, *Corros Sci* **2020**, *176*.

12. Desigan, N.; Ganesh, S.; Pandey, N. K.: Dissolution behavior of fast reactor MOX nuclear fuel pellets in nitric acid medium, *J Nucl Mater* **2021**, *554*.

13. Desigan, N.; Maji, D.; Ananthasivan, K.; Pandey, N. K.; Mudali, U. K.; Joshi, J. B.: Dissolution behaviour of simulated MOX nuclear fuel pellets in nitric acid medium, *Prog Nucl Energ* **2019**, *116*, 1-9.

14. Serrano, J. A.; Glatz, J. P.; Toscano, E. H.; Papaioannou, D.; Barrero, J.; Coquerelle, M.: Influence of low temperature air oxidation on the dissolution behaviour of UO$_2$ and MOX spent fuel, *J Alloy Compd* **1998**, *271*, 573-576.

15. Ziouane, Y.; Arab-Chapelet, B.; Leturcq, G.: Impact of the plutonium content on dissolution kinetics of (U$_{1-x}$Pu$_x$)O$_{2\pm\delta}$ powders, *Hydrometallurgy* **2020**, *198*.

16. Degueldre, C.; Pin, S.; Poonoosamy, J.; Kulik, D. A.: Redox state of plutonium in irradiated mixed oxide fuels, *J Phys Chem Solids* **2014**, *75*, 358-365.

17. Vauchy, R.; Robisson, A. C.; Belin, R. C.; Martin, P. M.; Scheinost, A. C.; Hodaj, F.: Room-temperature oxidation of hypostoichiometric uranium plutonium mixed oxides U$_{1-y}$Pu$_y$O$_{2-x}$ - A depth-selective approach, *J Nucl Mater* **2015**, *465*, 349-357.

18. Kim, H. S.; Joung, C. Y.; Lee, B. H.; Oh, J. Y.; Koo, Y. H.; Heimgartner, P.: Applicability of CeO$_2$ as a surrogate for PuO$_2$ in a MOX fuel development, *J Nucl Mater* **2008**, *378*, 98-104.

19. Shannon, R. D.: Revised Effective Ionic-Radii and Systematic Studies of Interatomic Distances in Halides and Chalcogenides, *Acta Crystallogr A* **1976**, *32*, 751-767.

20. Krishnan, R. V.; Panneerselvam, G.; Singh, B. M.; Kothandaraman, B.; Jogeswararao, G.; Antony, M. P.; Nagarajan, K.: Synthesis, characterization and thermal expansion measurements on uranium-cerium mixed oxides, *J Nucl Mater* **2011**, *414*, 393-398.

21. Martinez, J.; Clavier, N.; Mesbah, A.; Audubert, F.; Le Goff, X. F.; Vigier, N.; Dacheux, N.: An original precipitation route toward the preparation and the sintering of highly reactive uranium cerium dioxide powders, *J Nucl Mater* **2015**, *462*, 173-181.

22. Eloirdi, R.; Cakir, P.; Huber, F.; Seibert, A.; Konings, R.; Gouder, T.: X-ray photoelectron spectroscopy study of the reduction and oxidation of uranium and cerium single oxide compared to (U-Ce) mixed oxide films, *Appl Surf Sci* **2018**, *457*, 566-571.

23. Kulyako, Y. M.; Vinokurov, S. E.; Trofimov, T. I.; Pilyushenko, K. S.; Malikov, D. A.; Perevalov, S. A.; Savel'ev, B. V.; Dvoeglazov, K. N.; Shadrin, A. Y.; Myasoedov, B. F.: Preparation of Solid Solutions of Uranium and Cerium Oxides from Their Nitric Acid Solutions Using Microwave Radiation, *Radiochemistry+* **2019**, *61*, 661-664.

24. Tocino, F.; Szenknect, S.; Mesbah, A.; Clavier, N.; Dacheux, N.: Dissolution of uranium mixed oxides: The role of oxygen vacancies vs the redox reactions, *Prog Nucl Energ* **2014,** *72*, 101-106.

25. Herrero, B.; Bes, R.; Audubert, F.; Clavier, N.; Hunault, M. O. J. Y.; Baldinozzi, G.: Charge compensation mechanisms in Nd-doped UO_2 samples for stoichiometric and hypo-stoichiometric conditions: Lack of miscibility gap, *J Nucl Mater* **2020,** *539*.

26. Prieur, D.; Vigier, J. F.; Popa, K.; Walter, O.; Dieste, O.; Varga, Z.; Beck, A.; Vitova, T.; Scheinost, A. C.; Martin, P. M.: Charge Distribution in $U_{1-x}Ce_xO_{2+y}$ Nanoparticles, *Inorg Chem* **2021,** *60*, 14550-14556.

27. Trillaud, V.; Maynadie, J.; Manaud, J.; Hidalgo, J.; Meyer, D.; Podor, R.; Dacheux, N.; Clavier, N.: Synthesis of size-controlled UO_2 microspheres from the hydrothermal conversion of U(IV) aspartate, *Crystengcomm* **2018,** *20*, 7749-7760.

28. Rai, D.; Felmy, A. R.; Ryan, J. L.: Uranium(IV) Hydrolysis Constants and Solubility Product of $UO_2.xH_2O(am)$, *Inorg Chem* **1990,** *29*, 260-264.

29. Thompson, P.; Cox, D. E.; Hastings, J. B.: Rietveld Refinement of Debye-Scherrer Synchrotron X-Ray Data from Al_2O_3, *J Appl Crystallogr* **1987,** *20*, 79-83.

30. Frontera, C.; Rodriguez-Carvajal, J.: FullProf as a new tool for flipping ratio analysis, *Physica B: Condensed Matter* **2003,** *335*, 219-222.

31. Sitaud, B.; Solari, P. L.; Schlutig, S.; Llorens, I.; Hermange, H.: Characterization of radioactive materials using the MARS beamline at the synchrotron SOLEIL, *J Nucl Mater* **2012,** *425*, 238-243.

32. LLorens, I.; Solari, P. L.; Sitaud, B.; Bes, R.; Cammelli, S.; Hermange, H.; Othmane, G.; Safi, S.; Moisy, P.; Wahu, S.; Bresson, C.; Schlegel, M. L.; Menut, D.; Bechade, J. L.; Martin, P.; Hazemann, J. L.; Proux, O.; Den Auwer, C.: X-ray absorption spectroscopy investigations on radioactive matter using MARS beamline at SOLEIL synchrotron, *Radiochim Acta* **2014,** *102*, 957-972.

33. Ravel, B.; Newville, M.: ATHENA, ARTEMIS, HEPHAESTUS: data analysis for X-ray absorption spectroscopy using IFEFFIT, *J Synchrotron Radiat* **2005,** *12*, 537-541.

34. Kvashnina, K. O.; Butorin, S. M.; Martin, P.; Glatzel, P.: Chemical State of Complex Uranium Oxides, *Phys Rev Lett* **2013,** *111*, 253002.

35. Scheinost, A. C.; Claussner, J.; Exner, J.; Feig, M.; Findeisen, S.; Hennig, C.; Kvashnina, K. O.; Naudet, D.; Prieur, D.; Rossberg, A.; Schmidt, M.; Qiu, C. R.; Colomp, P.; Cohen, C.; Dettona, E.; Dyadkin, V.; Stumpf, T.: ROBL-II at ESRF: a synchrotron toolbox for actinide research, *J Synchrotron Radiat* **2021,** *28*, 333-349.

36. Martin, P.; Ripert, M.; Petit, T.; Reich, T.; Hennig, C.; D'Acapito, F.; Hazemann, J. L.; Proux, O.: A XAS study of the local environments of cations in (U, Ce)O_2, *J Nucl Mater* **2003,** *312*, 103-110.

37. Epifano, E.; Naji, M.; Manara, D.; Scheinost, A. C.; Hennig, C.; Lechelle, J.; Konings, R. J. M.; Gueneau, C.; Prieur, D.; Vitova, T.; Dardenne, K.; Rothe, J.; Martin, P. M.: Extreme multi-valence states in mixed actinide oxides, *Commun Chem* **2019,** *2*.

38. Leinders, G.; Cardinaels, T.; Binnemans, K.; Verwerft, M.: Accurate lattice parameter measurements of stoichiometric uranium dioxide, *J Nucl Mater* **2015,** *459*, 135-142.

39. Artini, C.; Pani, M.; Carnasciali, M. M.; Buscaglia, M. T.; Plaisier, J. R.; Costa, G. A.: Structural Features of Sm- and Gd-Doped Ceria Studied by Synchrotron X-ray Diffraction and μ-Raman Spectroscopy, *Inorg Chem* **2015,** *54*, 4126-4137.

40. Devi, K. V. V.; Ramkumar, J.; Biju, K.; Sathe, D. B.: Plutonium heterogeneity in MOX fuel: A quantitative analysis, *J Nucl Mater* **2019,** *518*, 129-139.

41. Claparede, L.; Clavier, N.; Mesbah, A.; Tocino, F.; Szenknect, S.; Ravaux, J.; Dacheux, N.: Impact of the cationic homogeneity on $Th_{0.5}U_{0.5}O_2$ densification and chemical durability, *J Nucl Mater* **2019,** *514*, 368-379.

42. Abraham, F.; Arab-Chapelet, B.; Rivenet, M.; Tamain, C.; Grandjean, S.: Actinide oxalates, solid state structures and applications, *Coordin Chem Rev* **2014**, *266*, 28-68.

43. Manaud, J.; Maynadie, J.; Mesbah, A.; Hunault, M. O. J. Y.; Martin, P. M.; Zunino, M.; Meyer, D.; Dacheux, N.; Clavier, N.: Hydrothermal Conversion of Uranium(IV) Oxalate into Oxides: A Comprehensive Study, *Inorg Chem* **2020**, *59*, 3260-3273.

44. Desfougeres, L.; Welcomme, E.; Ollivier, M.; Martin, P. M.; Hennuyer, J.; Hunault, M. O. J. Y.; Podor, R.; Clavier, N.; Favergeon, L.: Oxidation as an Early Stage in the Multistep Thermal Decomposition of Uranium(IV) Oxalate into U_3O_8, *Inorg Chem* **2020**, *59*, 8589-8602.

45. Bregiroux, D.; Terra, O.; Audubert, F.; Dacheux, N.; Serin, V.; Podor, R.; Bernache-Assollant, D.: Solid-state synthesis of monazite-type compounds containing tetravalent elements, *Inorg Chem* **2007**, *46*, 10372-10382.

46. Riess, I.; Janczikowski, H.; Nolting, J.: O_2 Chemical Potential of Non-stoichiometric Ceria, CeO_{2-x}, Determined by a Solid Electrochemical Method, *J Appl Phys* **1987**, *61*, 4931-4933.

47. Bes, R.; Kvashnina, K.; Rossberg, A.; Dottavio, G.; Desgranges, L.; Pontillon, Y.; Solari, P. L.; Butorin, S. M.; Martin, P.: New insight in the uranium valence state determination in $U_yNd_{1-y}O_{2\pm x}$, *J Nucl Mater* **2018**, *507*, 145-150.

48. Fouquet-Metivier, P. Study of the influence of americium on thermodynamic and structural properties of $(U,Pu)O_{2\pm x}$ mixed oxides. Université Paris-Saclay, 2022.

49. Markin, T. L.; Street, R. S.; Crouch, E. C.: Uranium-Cerium-Oxygen Ternary Phase Diagram, *J Inorg Nucl Chem* **1970**, *32*, 59-&.

50. Manaud, J.; Maynadie, J.; Mesbah, A.; Hunault, M. O. J. Y.; Martin, P.; Zunino, M.; Dacheux, N.; Clavier, N.: Hydrothermal Conversion of Thorium Oxalate into into $ThO_2 \cdot nH_2O$ oxide, *Inorg Chem* **2020**, *59*, 14954-14966.

51. Tagawa, H.; Fujino, T.; Watanabe, K.; Nakagawa, Y.; Saita, K.: Oxidation-Reduction Properties of Mixed Oxides in the Cerium-Uranium-Oxygen System, *B Chem Soc Jpn* **1981**, *54*, 138-142.

52. Lorenzelli, R.; Touzelin, B.: The System UO_2-CeO_2 - High-Temperature Crystallographic Study, *J Nucl Mater* **1980**, *95*, 290-302.

53. Nawada, H. P.; Sriramamurti, P.; Kutty, K. V. G.; Rajagopalan, S.; Yadav, R. B.; Rao, P. R. V.; Mathews, C. K.: Oxidation and Phase-Behavior Studies of the U-Ce-O System, *J Nucl Mater* **1986**, *139*, 19-26.

54. Dorr, W.; Hellmann, S.; Mages, G.: Study of the Formation of UO_2-PuO_2 Solid-Solution by Means of UO_2-CeO_2 Simulate, *J Nucl Mater* **1986**, *140*, 7-10.

55. Krishnan, R. V.; Nagarajan, K.: Heat capacity measurements on uranium-cerium mixed oxides by differential scanning calorimetry, *Thermochim Acta* **2006**, *440*, 141-145.

56. Nagarajan, K.; Saha, R.; Yadav, R. B.; Rajagopalan, S.; Kutty, K. V. G.; Saibaba, M.; Rao, P. R. V.; Mathews, C. K.: Oxygen Potential Studies on Hypostoichiometric Uranium-Cerium Mixed-Oxide, *J Nucl Mater* **1985**, *130*, 242-249.

57. Kim, D. J.; Lee, Y. W.; Kim, Y. S.: The thermal conductivity and lattice parameter measurements in a low Ce content $(U_{1-y}Ce_y)O_2$ mixed oxide, *J Nucl Mater* **2005**, *342*, 192-196.

58. Cao, H. J.; Bao, H. L.; Lin, X.; Lin, J.; Zhang, L. J.; Huang, Y. Y.; Wang, J. Q.: Differential interplay between Ce and U on local structures of $U_{1-x}Ce_xO_2$ solid solutions probed by X-ray absorption spectroscopy, *J Nucl Mater* **2019**, *515*, 238-244.

59. Kurosaki, K.; Ohshima, R.; Uno, M.; Yamanaka, S.; Yamamoto, K.; Namekawa, T.: Thermal conductivity of $(U,Ce)O_2$ with and without Nd or Zr, *J Nucl Mater* **2001**, *294*, 193-197.

60. Prieur, D.; Desagulier, M. M.; Neuville, D. R.; Gueneau, C.; Epifano, E.; Dardenne, K.; Rothe, J.; Martin, P.: A spectroscopic hike in the U-O phase diagram, *J Synchrotron Radiat* **2021,** *28*, 1684-1691.

61. Zinkevich, M.; Djurovic, D.; Aldinger, F.: Thermodynamic modelling of the cerium-oxygen system, *Solid State Ionics* **2006,** *177*, 989-1001.

62. Sali, S. K.; Keskar, M.; Phatak, R.; Krishnan, K.; Shelke, G. P.; Shafeeq, P. P. M.; Kannan, S.: Oxidation behavior of $(U_{1-y}Ce_y)O_{2.00}$; (y=0.21, 0.28 and 0.44) solid solutions under different oxygen potentials. Thermogravimetric and in situ X-ray diffraction studies, *J Nucl Mater* **2018,** *510*, 499-512.

63. Duriez, C.; Alessandri, J. P.; Gervais, T.; Philipponneau, Y.: Thermal conductivity of hypostoichiometric low Pu content $(U,Pu)O_{2-x}$ mixed oxide, *J Nucl Mater* **2000,** *277*, 143-158.

Table of Contents graphic
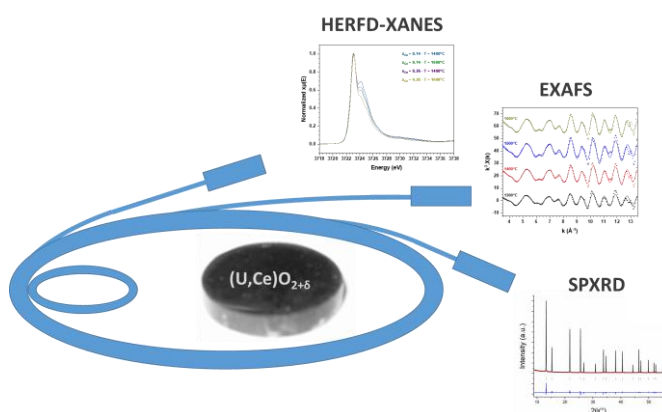
Synopsis

This paper reports the synchrotron investigation of homogeneous $(U,Ce)O_{2+\delta}$ oxides sintered in various atmospheres. Under reducing conditions, O/M ratio appeared close to 2.00 using HERFD-XANES, while it was hyper-stoichiometric under argon, and decreased with the cerium content and the sintering temperature. Such deviation was found to generate moderate structural disorder from EXAFS. Finally, Synchrotron-PXRD data led to propose a mathematic expression linking the unit cell parameter, the chemical composition and the deviation from the stoichiometry.